ACS APPLIED ENERGY MATERIALS

www.acsaem.org Article

Selective Electrooxidation of Glycerol to Formic Acid over Carbon Supported $Ni_{1-x}M_x$ (M = Bi, Pd, and Au) Nanocatalysts and Coelectrolysis of CO_2

Mohamed S. E. Houache, Reza Safari, Uzoma O. Nwabara, Thibault Rafaïdeen, Gianluigi A. Botton, Paul J. A. Kenis, Stève Baranton, Christophe Coutanceau, and Elena A. Baranova*

Cite This: *ACS Appl. Energy Mater.* 2020, 3, 8725−8738 Read Online

ACCESS | Metrics & More | Article Recommendations | Supporting Information

ABSTRACT: The composition effect of carbon supported Ni_xM_{1-x} (M = Bi, Pd, and Au) nanomaterials toward glycerol electrooxidation (GEOR) was evaluated in alkaline media. Ni-rich catalysts with different atomic ratios (M atomic ratio ≤20%) were synthesized by the heatless coreduction method and characterized by various physicochemical and electrochemical techniques. All structures of the Ni_xM_{1-x}/C catalysts were composed of a rich phase of $Ni(OH)_2$, as evidenced by TDA-TGA and XPS. Among the different nanomaterials, the $Ni_{0.9}Au_{0.1}/C$ catalyst provided the lowest onset potential (+0.12 V vs Hg/HgO) and the highest peak current density. *In situ* infrared spectroscopy experiments combined with electrochemical measurements exhibited the formation of formate for all catalysts, thus indicating the breakage of C−C bonds of glycerol. GEOR led to 100% selectivity for formate after 1 h electrolysis and 100% conversion of glycerol after 24 h at +1.55 V. Furthermore, when these inexpensive catalysts were tested in tandem with cathodic CO_2 electroreduction, the anodic $Ni_{0.9}Au_{0.1}/C$ catalyst displayed the highest partial current density for CO and the lowest onset potential.

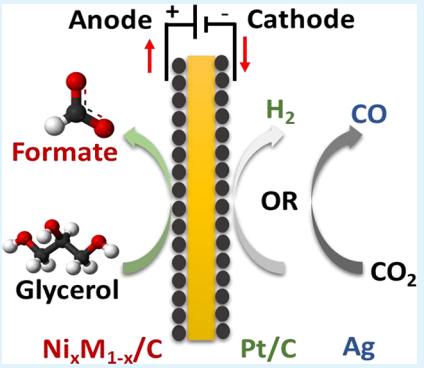

KEYWORDS: *Ni-based catalysts, glycerol, electrolysis, selectivity, CO_2 electroreduction*

1. INTRODUCTION

Continuous efforts have been devoted to developing efficient electrochemical conversion technologies to generate energy and/or value-added products from oxygenated biomass such as glucose, furfural, xylose, and glycerol.[1−4] Particularly, glycerol (byproduct of biodiesel production) is one of the top 12 platform compounds and has great potential to be transformed into more economical products such as glyceric, tartronic, lactic, and formic acids.[5] Among various technologies being studied for glycerol valorization, electrochemical technologies are more promising due to straightforward operation, are environmentally friendly, and require low operating temperatures and pressures.[6] Furthermore, the electrocatalytic oxidation processes of glycerol on the anode of either a fuel or electrolysis cell is tunable by means of electrode potential, surface crystallinity, electrocatalyst composition, i.e., nanoparticles with defined morphologies and core−shell structures, and utilization of different support materials.[7] Controlling these parameters could lead to a lower oxidation onset potential and a higher product selectivity at high conversion, and in return a cheaper process is achieved.

Thermodynamic data indicate that the use of glycerol as anodic reactant in an electrolysis cell could be more energetically interesting than water electrolysis for hydrogen production.[8] This is due to lower theoretical cell voltage for glycerol electrolysis (U^0_{cell} = 0.003 V, n = 14 for the complete oxidation of glycerol into CO_2) compared to water electrolysis (U^0_{cell} = +1.229 V, n = 2), where n is the number of electrons generated per molecule oxidized.[9] However, the main limitation in using glycerol as a hydrogen source is the slow kinetics of its oxidation reaction. For this purpose, alkaline media was favored over acidic media, leading to faster electrochemical kinetics and allowing using free or low loaded Pt-group metal catalysts for both reactions: glycerol electrooxidation at the anode and H_2 evolution at the cathode.[10−12] Another interesting approach is the coelectrolysis of glycerol and CO_2 as a pathway to value-added chemicals. Currently, CO_2 electroreduction processes are comprised of the anodic oxygen evolution reaction (OER) coupled to the cathodic CO_2 reduction. Thermodynamic analysis indicates that OER requires ∼90% of the electricity consumption because of high anodic potential (cell voltage of ∼−1.6 V) on the Pt black electrode.[13] However, altering the anodic OER to the glycerol

Received: June 3, 2020
Accepted: August 3, 2020
Published: August 3, 2020

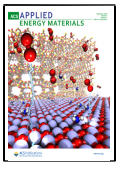

https://dx.doi.org/10.1021/acsaem.0c01282
ACS Appl. Energy Mater. 2020, 3, 8725−8738

electro-oxidation reaction (GEOR) results in lowering the CO_2 electroreduction cell voltage by ∼−0.85 V with 37−53% reduction in electricity requirements, thus improving its feasibility.

Regardless of the significant advances made during the past two decades in the fuel cell and electrolysis cell technology, the anodic current performance for glycerol electro-reforming is not yet close to attaining the widespread commercialization targets based on the United States Department of Energy (DOE).[14,15] Currently, many efforts have been devoted to developing non-Pt group metal catalysts to minimize the cost and enhance the performance of electrochemical technologies. Among various electrode materials, nickel (Ni) is considered as one of the most promising nonprecious electrocatalytic material and has been utilized in several electrochemical applications such as alkaline batteries, sensors, alcohol oxidation, and fuel cells.[16−21] This attraction is due to nickel's low preparation cost, long-term stability, resistance to CO poisoning, and high surface oxidation performance by the formation of high valence oxyhydroxide species (β-NiOOH) in an alkaline medium.[22−25] Nonetheless, the poor electrical conduction of these Ni^{3+} species and agglomeration of small Ni nanoparticles (NPs) seriously limit their catalytic performance.[26] To overcome these issues, Ni NPs can be immobilized and dispersed on a two-dimensional solid support, typically high specific surface area electron conductive carbon materials.[27] The electrocatalytic performance of the resulting nanocomposites can be enhanced significantly due to high conductive matrices, fast electron transfer kinetics, and high surface area with abundant active sites.[28−30]

In this context, developing and finding highly stable and active electrocatalysts is of great significance for promoting GEOR in the electrolysis cells operating at low temperature. Other promising approaches for Ni catalysts have been suggested, such as compositing or alloying with other catalytic elements. The modifying effect of noble metals by nickel can provide a lot of information for understanding catalytic kinetics for GEOR and designing more stable and active catalysts. For instance, Au/Ni on polystyrene spheres[31] and Pt_2Ni_1/C and Pd_6Ni_4/C materials[32] led to higher catalytic activity and stability in comparison to the monometallic ones. This enhancement can be ascribed to electronic and geometric modifications.[33] Ni, an oxophilic metal like ruthenium (Ru), possesses the unique capability of generating efficient OH_{ads} at lower overpotential and thus facilitates oxidative desorption of the intermediates,[34] corresponding to the so-called bifunctional mechanism of electrocatalysis.[35] Therefore, the transition metal (Ni) served as a promoter and was able to reduce the precious metal amounts without significantly affecting the catalytic performance. However, only few studies have been devoted to the electro-oxidation of biomass-derived glycerol using Ni-rich alloyed catalysts, the topic of this study.

Here we demonstrate carbon supported Ni_xM_{1-x} (M = Bi, Pd, and Au) nanoparticles (NPs) with different atomic ratios prepared using the straightforward sodium borohydride ($NaBH_4$) coreduction method. Addition of small quantities of second metal (≤20 at. %) had a positive effect on catalytic performance with a lower onset potential and long durability up to 24 h. Detailed analyses of product distribution revealed that Ni_xM_{1-x}/C catalysts own high capacities to cleave the C−C bond of glycerol, generating 100% selectivity toward formate with 100% conversion of glycerol at +1.55 V. Lastly, coelectrolysis of CO_2 and the glycerol process were introduced, showing that the $Ni_{0.9}Au_{0.1}$/C catalyst attained the highest partial current density for CO of ∼6.0 mA cm^{-2} and lowest onset cell voltage of −1.0 V. To our knowledge, no work has been reported in the literature on coelectrolysis of glycerol and CO_2 using Ni-rich anode catalysts for such a process.

2. EXPERIMENTAL SECTION

2.1. Prepartation of Ni_xM_{1-x} (M = Pd, Au, and Bi) Nanoparticles. All carbon supported Ni, Ni_xPd_{1-x} (atomic ratio x = 0.95, 0.90, 0.80), Ni_xAu_{1-x}, and Ni_xBi_{1-x} (atomic ratio x = 0.98, 0.95, 0.90) NPs were prepared by the sodium borohydride ($NaBH_4$) coreduction method at room temperature from metal chloride salt without any capping agent. The detailed procedure of this method was reported elsewhere for unsupported Ni.[36] After 30 min of metal reduction, a given amount of carbon powder (Vulcan XC72, Cabot Corp.) was introduced to the solution to attain 30 wt % of metal loading. The colloidal mixture was filtered and rinsed three times with acetone. The catalytic residue was dried in an oven at 313 K for 15 h.

2.2. Physicochemical Characterizations. All detailed procedures of different physicochemical techniques (XRD, TEM, SAED, HAADF, EDS, and EELS) have been reported earlier in our previous publication.[37] Thermogravimetric analyses (TGA/DTA, TA Instruments model SDT Q 600 apparatus) were performed to determine the metal loadings. The catalyst powders were gradually heated in alumina crucible from 25 to 1050 °C with an air flow of 100 mL min^{-1} and a heating rate of 10 K min^{-1}. An empty alumina crucible was used as reference. XPS spectra were collected by using a Kratos Axis ULTRA X-ray photoelectron spectrometer with monochromatic Al Kα excitation. The binding energy (BE) scale was assigned by adjusting the C 1s peak at 284.6 eV.

2.3. Electrochemical Measurements. The electrochemical setup composed of a conventional three-electrode thermostated cell fitted with a mercury/mercury oxide (Hg/HgO) reference electrode as well as a glassy carbon (GC) disk (0.071 cm^2) and a glassy carbon plate (4 cm^2 surface area) which acted as a working electrode and a counter electrode, respectively. The linear sweep voltammetry (LSV) and cyclic voltammetry (CV) measurements were performed using a Voltalab PGZ402 potentiostat (Radiometer Analytical) in a N_2-purged 1.0 M KOH (99.99%, Sigma-Aldrich) and 0.1 M glycerol (99.98%, Sigma-Aldrich) electrolyte at 293 K. Prior to electrochemical measurements, a catalytic ink was prepared as follows: 17.7 mg of Ni_xM_{1-x}/C (M = Pd, Au, and Bi) materials was added to aqueous suspension of 2.117 mL of ultrapure water (Milli-Q Millipore, 18.2 MΩ cm at 293 K), 0.674 mL of isopropanol (CHROMASOLV LC-MS, Fluka Analytical), and 354 μL of commercial solution of Nafion (5 wt % in aliphatic alcohols, Sigma-Aldrich). The prepared ink was homogenized for 2 min, and 3 μL was deposited onto the glassy carbon disk.

2.4. *In Situ* Fourier Transform Infrared Spectroscopy (FTIRS) Measurements. *In-situ* FTIRS measurements were performed on a Bruker IFS 66v/S FTIR spectrometer with a reflected beam at a 65° incident angle on the electrode surface. The chamber was under vacuum to eliminate the CO_2 and atmospheric water interferences from the beam path. The detector was HgCdTe type, cooled beforehand by liquid nitrogen. All the measurements were performed in a special tailored spectroelectrochemical cell fitted with a CaF_2 prism at the bottom. The spectrum was acquired by averaging 512 interferograms with 4 cm^{-1} resolution. Sample spectra were recorded every 50 s during LSV performed in a 0.1 or 1.0 M KOH and 0.1 M glycerol solution from −0.900 to +0.775 V vs Hg/HgO at a scan rate of 1 mV s^{-1}. Data were processed as follows:[1,8]

$$\frac{\Delta R}{R} = \frac{R_E - R_{E,ref}}{R_{E,ref}} \quad (1)$$

where R_E is the reflectivity recorded at the electrode potential E during the positive potential scan and $R_{E,ref}$ is the reflectivity used as reference recorded at −0.900 V vs Hg/HgO. Negative- and positive-

https://dx.doi.org/10.1021/acsaem.0c01282
ACS Appl. Energy Mater. 2020, 3, 8725−8738

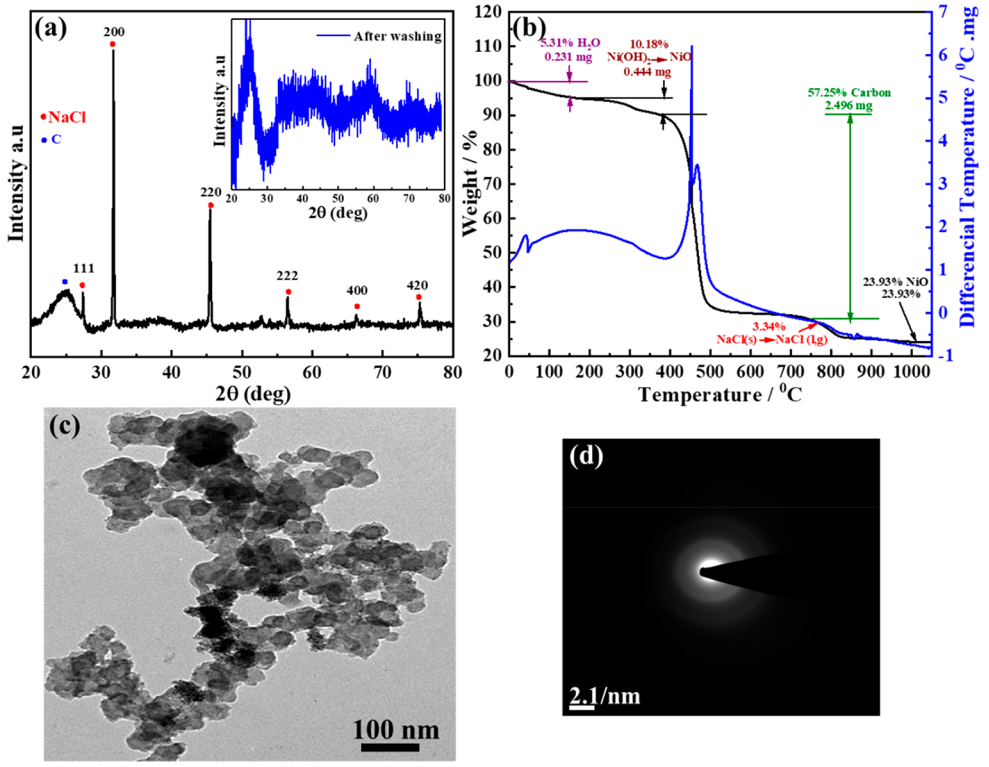

Figure 1. (a) XRD pattern of Ni/C, (b) TGA/DTA measurements of Ni/C (metal loading: 30 wt %) in temperature range 25−1050 °C, (c) TEM image, and (d) amorphous SAED patterns of Ni/C.

going bands represent respectively the increase and decrease of species at the electrode surface.

2.5. Continuous Electrolysis Measurements. Continuous electrolysis tests were performed at 293 K with a 1.0 M KOH and 0.1 M glycerol aqueous solution in a 25 cm^2 electrolysis cell. The anode and the cathode were composed of 2 mg_{metal} cm^{-2} of carbon supported Ni-based catalysts Ni_xM_{1-x}/C (M = Pd, Au, and Bi) and Pt/C, respectively, and the Nafion (as binder) loading of the electrode was 0.8 mg cm^{-2} in deionized water and isopropanol. Both compartments were separated by a simple filter paper (Whatman) and mechanically compressed in the cell.

A DC power supply (E3614A from Agilent) and digital multimeters (34405A from Agilent) were used to applied and measure the cell voltage and to record the current crossing the cell, respectively. A 30 mL solution (1.0 M KOH + 0.1 M glycerol) was fed continuously on both compartments at 30 mL min^{-1}. The current was recorded for 24 h at two different cell voltages of +1.30 and +1.55 V.

An HPLC (Varian Prostar) equipped with a column (Transgenomc ICSep ICE-COREGEL 107H) was utilized to analyze the products at each hour for 6 h with the UV detector set at λ = 210 nm. The chromatography was performed with a 7 mM H_2SO_4 aqueous solution with 0.6 mL min^{-1} flow rate. The last solutions at 24 h were neutralized by HCl, freeze-dried, and put in deuterium oxide (D_2O, 99.9% purity, Sigma-Aldrich) for analysis in ^1H NMR (Bruker Ultrashield 400 plus with a Bruker B-ACS 60 automatic sample changer and a Bruker AD-XT pump).

2.6. Electrode Preparation for Coelectrolysis of CO_2 and Glycerol. Commercially available silver (<100 nm, Sigma-Aldrich, product number: 576832) was used as the cathode catalysts to study CO_2 electroreduction to CO. The as-prepared Ni-based bimetallics, as well as commercial Pt (<100 nm, Alfa Aesar, product number: 43838) and Au (<100 nm, Sigma-Aldrich, product number: 636347) controls, were used as anode catalyst for GEOR. To prepare the Ag cathodes and Ni_xM_{1-x}/C anodes, about 10 mg of the catalyst powder was weighed out in a glass vial. 500 μL of deionized water (DI, Barnstead E-pure) and 9 mL of DI water were added to the Ag catalyst vial and Ni alloy catalyst vial, respectively. Then, 26 μL of Nafion ionomer (5 wt %, Fuel Cell Earth) was added to the vial with the catalyst powder. Finally, 1 mL of isopropyl alcohol (IPA, Fisher Chemical) was added to the Ag catalyst vial, and 9 mL of IPA was added to the Ni catalyst vial. For preparing the control anodes, about 3 mg of catalyst powder (either Pt or Au) was weighed out followed by the addition of 300 μL of DI water, 7.8 μL of Nafion, and 700 μL of IPA. The mixture was then sonicated by using a probe sonicator to form a cohesive catalyst ink. The ink was then airbrushed onto a 5 × 1 cm^2 gas diffusion electrode (Sigracet 35BC, Fuel Cell Store), corresponding to two electrodes, by using an airbrushing setup described previously.[38] Close to 50% of the original catalysts is lost during airbrushing, resulting in a final loading of 1.0 ± 0.1 mg cm^{-2} for the Ag and Ni bimetallic electrodes and 0.3 ± 0.03 mg cm^{-2} for the Pt and Au.

2.7. Coelectrolysis of CO_2 and Glycerol in a Flow Electrolyzer. The airbrushed electrodes (preparation of electrode is in the Supporting Information) were tested in a flow electrolyzer, as previously reported.[13] CO_2 (Airgas) was constantly fed to the backside of the Ag NPs cathode at a flow rate of 17 sccm by using a flow controller (Smart-Trak 2, Sierra Instruments), whereas the GEOR was performed on Ni_xM_{1-x}/C at the anode. CO_2 electroreduction on Ag produces CO, H_2, and traces of formate.[39] Both catholyte (2.0 M KOH, Fisher Chemical) and anolyte (2.0 M KOH + 2.0 M glycerol, Fisher Chemical) were constantly flowed at 0.5 mL min^{-1} via a syringe pump (PHD 2000, Harvard Apparatus) to electrolyte chambers separated by an anion exchange membrane (FAA-3-PK-75, Fumatech). The electrolyzer was operated potentiostatically; the cell voltages (−1.50, −1.40, −1.30, −1.20, −1.10, −1.00, −0.90, −0.80, and −0.75 V) were applied, and the corresponding currents were measured by an Autolab PGSTAT-30, EcoChemie potentiostat. Multimeters (Crenova MS8233D) were used to measure cathode and anode potentials against Ag/AgCl reference electrodes (3 mol kg^{-1}, RE-5B BASi). At each cell voltage, the system was left to equilibrate for 200 s before taking injections via a gas chromatograph (Thermo Finnigan Trace GC) equipped with a thermal conductivity detector to measure any gaseous products. A pressure regulator (Cole Parmer, 00268TC) connected to a vacuum pump was placed

https://dx.doi.org/10.1021/acsaem.0c01282
ACS Appl. Energy Mater. 2020, 3, 8725−8738

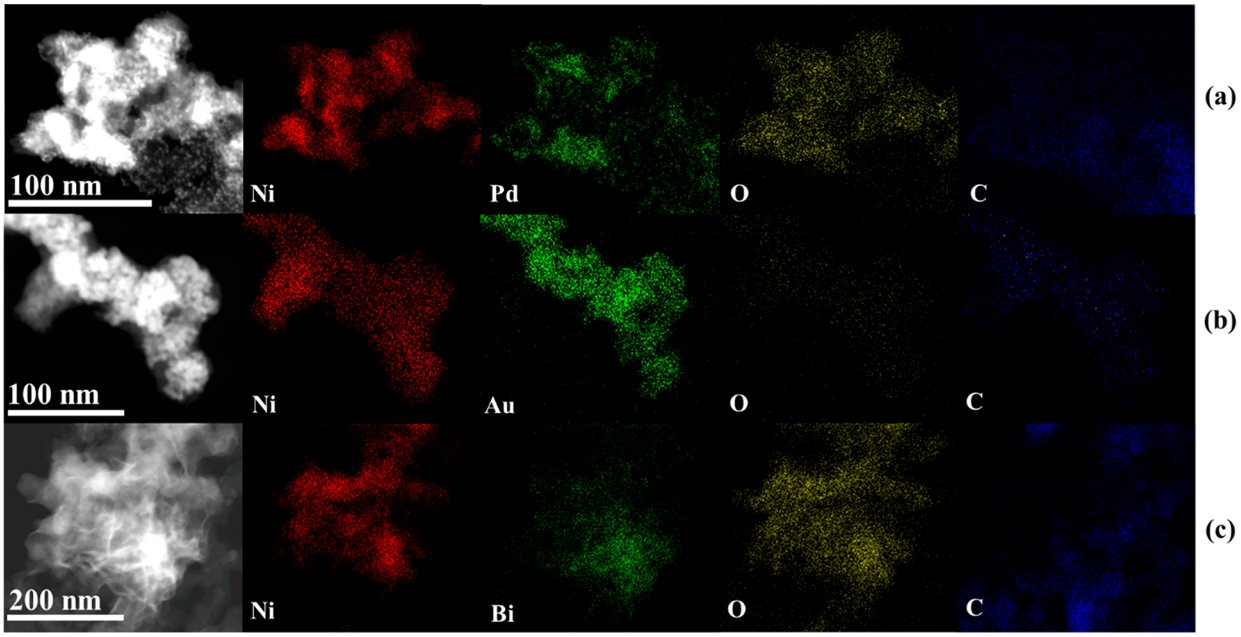

Figure 2. Dark-field STEM image and EDS mapping of Ni, Pd, Au, O, and C of carbon supported Ni-based catalysts (a) $Ni_{0.8}Pd_{0.2}/C$, (b) $Ni_{0.9}Au_{0.1}/C$, and (c) $Ni_{0.9}Bi_{0.1}/C$.

downstream of the GC and set to 14.20 psi to help facilitate gaseous product transfer from the cathode surface to the effluent gas stream. Liquid samples were taken from the anolyte to be analyzed for liquid products by using ^{1}H NMR.

3. RESULTS AND DISCUSSION

3.1. Physicochemical Characterization of Ni_xM_{1-x}/C Materials. Physicochemical characterizations were performed to obtain information about the composition and structure of Ni_xM_{1-x}/C materials.

XRD patterns of as-prepared Ni/C and Ni_xM_{1-x}/C NPs (M = Pd, Au, and Bi) of different ratios are presented in Figure 1a and Figure S1a–c). Six intense peaks were observed. These sharp peaks indicate that pure NaCl crystallized in the cubic system with the *Fm*3*m* symmetry space group as stated in the JCPDS 05-0628 card.[40] The formation of NaCl is explained by the presence of chlorides anions from the metal salt used as precursors and of sodium cations brought by addition of sodium borohydride for the coreduction reaction, while a common peak was detected at ∼25°, which refers to turbostratic graphite (002) plane of the Vulcan carbon support.[41] However, no structural information about Ni or $Ni(OH)_2$ was detected, which could be due to the small size and/or amorphous nature of Ni-based materials and interference with NaCl phase.[40] The Ni/C sample was rinsed with ultrapure water, and the related XRD pattern is given in the inset of Figure 1a. After rinsing, the broadening diffraction peaks of low intensity illustrates an amorphous structure of Ni/C. It was also noticed in Figure S1a,b that Ni_xPd_{1-x}/C and Ni_xAu_{1-x}/C exhibited diffraction peaks located at the characteristic positions for a face-centered cubic (fcc) structure, typical of metallic Pd (111) and Au (111). The XRD patterns of Ni_xBi_{1-x}/C agree with (PDF-Nr.: 03-065-2366) data, confirming two reflection peaks of Bi_2O_3 (002) and (220) in the rhombohedral system (Figure S1c).[42]

Figure 1b and Figure S2a–c show the TGA/DTA plots for the as-prepared Ni-based materials. The relative mass percentage is plotted as a function of temperature, which detects a significant mass loss at five temperature intervals. The first transition below 200 °C corresponds to the elimination of adsorbed water on the catalyst powder. The second transition translates the metal oxides (NiO) formation in the range 200–340 °C and is ascribed to the dehydration of $Ni(OH)_2$.[41] Following this, the carbon support combustion is in the range 340–800 °C, and then the vaporization of NaCl molten salts occurs at 800.5 °C.[43] The remaining materials at the end of calcination (1050 °C) for all the catalysts are in the range from ∼24 to 35 wt %, which is in fair accordance with the initial target value of 30 wt % metal loading.

Typical TEM micrographs (Figure 1c and Figures S3–S11a) of all Ni_xM_{1-x}/C catalysts reveal the structural morphology of agglomerated NPs on carbon support with a network of small branches. However, because of the low contrast between Ni nanostructure and the carbon support, it is quite challenging to estimate the average particle size of the catalyst. In certain spots the grain size is ≤3 nm, which is significantly lower value than that obtained in our previous work on unsupported Ni-based materials.[37] Additionally, selected area electron diffraction (SAED) analysis reveals asset of full rings, indicating that Ni/C has no crystallization degree (Figure 1d), which agrees with our XRD data in Figure 1a.

To further characterize the Ni_xM_{1-x}/C materials with transition and post-transition-metal ions, HAADF-STEM, EDS, EDS mapping, and STEM-EELS analysis were performed. In Figure 2 and Figures S3–S11b–g, EDS mapping images confirm the presence of Ni (shown in red), O (shown in yellow), and C (shown in blue) and that the second metal, either Pd, Au, or Bi (shown in green), is well dispersed in the selected area of Ni_xM_{1-x}/C catalysts. The EDS spectra are also in accordance with the elemental composition of Ni_xM_{1-x}/C, as confirmed by the presence of the characteristic peaks of oxygen, palladium, gold, bismuth, and nickel. Furthermore, the chemical microstructures of the surfaces of the Ni-rich nanoparticles were also examined by using STEM-EELS analysis.

https://dx.doi.org/10.1021/acsaem.0c01282
ACS Appl. Energy Mater. 2020, 3, 8725–8738

Figure 3 illustrates the HAADF-STEM images for $Ni_{0.8}Pd_{0.2}/C$, $Ni_{0.9}Au_{0.1}/C$, and $Ni_{0.9}Bi_{0.1}/C$ catalysts. Figure 3

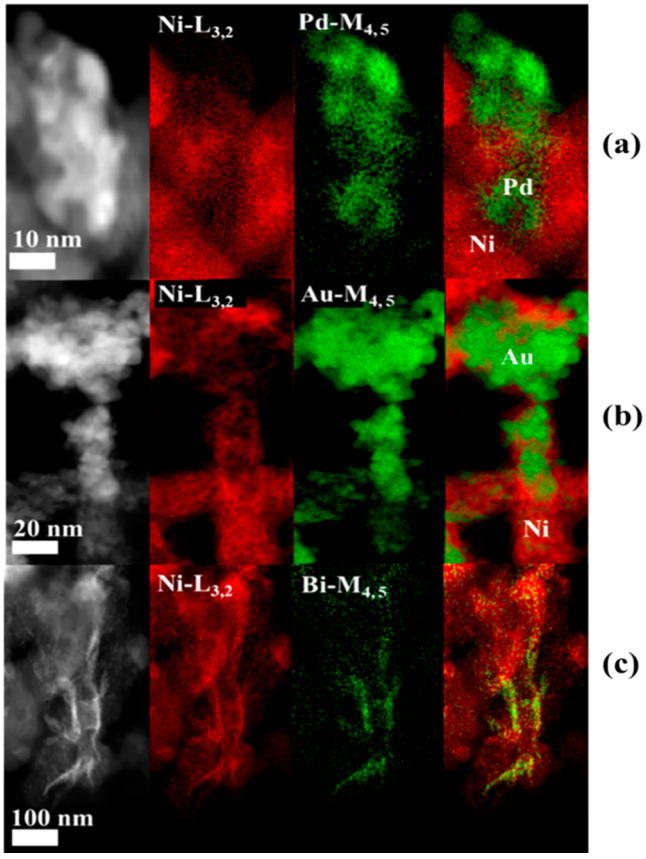

Figure 3. HAADF-STEM images and EELS map of Ni-$L_{2,3}$, Pd-$M_{4,5}$, Au-$M_{4,5}$, and Bi-$M_{4,5}$ of carbon supported Ni-based catalysts (metal loading: 30 wt %) (a) $Ni_{0.8}Pd_{0.2}/C$, (b) $Ni_{0.9}Au_{0.1}/C$, and (c) $Ni_{0.9}Bi_{0.1}/C$.

also shows the elemental distribution of Ni $L_{2,3}$, Pd−$M_{4,5}$, Au−$M_{4,5}$, and Bi−$M_{4,5}$ within the particle, which were extracted from different signals of ∼855, 400, 2200, and 2600 eV, respectively (Figure S12). The Ni (red) versus Pd, Au, and Bi (green) composite images indicate that the Pd, Au, and Bi atoms are surrounded by Ni atoms, indicating the Ni surface segregation in some areas. However, $Ni_{0.9}Bi_{0.1}/C$ (Figure 3c) adopted a nanoflake-like morphology varying remarkably from that seen for $Ni_{0.8}Pd_{0.2}/C$ and $Ni_{0.9}Au_{0.1}/C$ NPs.

Figure 4a−d depicts the XPS spectra of the Ni 2p, Pd 3d, Au 4f, and Bi 4f core level regions, respectively. The Ni/C XPS spectrum on the biding energy range corresponding to Ni $2p_{3/2}$ and Ni $2p_{1/2}$ shows two main peaks at 856.2 and 874.1 eV, respectively, and two satellite peaks located at 861.9 and 880.1 eV, respectively (Figure 4a). The spin−orbital splitting of the two main peaks is 17.9 eV, which is characteristic of a $Ni(OH)_2$ phase with no metallic Ni (852 eV).[44,45] The peak at 532.4 eV is assigned to O1 photoelectrons (Figure S13), comprised of O^{II} and O^{III}, which can be attributed to chemisorbed and physisorbed $Ni(OH)_2$ and molecular water or/and possibly adsorbed O_2, respectively.[45] In the Ni_xM_{1-x}/C (M = Pd, Au, and Bi) XPS spectra, one can see four peaks corresponding to Ni 2p and O 1s, exhibiting a slight shift compared to Ni/C (Table S1). In Figure 4b, the Pd 3d region is comprised of a doublet peaks centered at 337.8 and 343.4 eV (FWHM ≈ 2.29 ± 0.03 eV for both Pd 3d peaks along with spin−orbital splitting of 5.6 eV), in good correlation with the reported values for PdO_2.[46,47] Moreover, the Au 4f spectrum appears at lower range between 80 and 90 eV with two doublets Au $4f_{7/2}$ (84.2 eV) and Au $4f_{5/2}$ (87.9 eV) in Figure 4c. The position of the peaks indicates the formation of a pure metal gold (Au(0)) with the 3.7 eV binding energy distance and FWHM ≈ 1.3 ± 0.1 eV.[46,48] In Figure 4d, the two strong XPS peaks detected at binding energies of 159.7 and 165.0 eV were attributed to Bi $4f_{7/2}$ and Bi $4f_{5/2}$ of Bi^{3+} in Bi_2O_3 (FWHM ≈ 1.63 ± 0.03 eV) with 0.7 eV higher energy positions than pure Bi_2O_3.[49,50] This shift could be ascribed to the changes in the chemical environment caused by Ni addition.

3.2. Evaluation of the Catalytic Activity. Cyclic voltammograms (CV) recorded for Ni_xM_{1-x}/C materials (M = Pd, Au, and Bi) at 0.05 V s^{-1} in 1.0 M KOH aqueous electrolyte are illustrated in Figure 5a and Figure S14. The Ni^{II}/Ni^{III} redox process of the monometallic material is well established in our previous studies.[20,37,51] The reversible oxidation of β-$Ni(OH)_2$ to β-NiOOH takes place between +0.49 and +0.60 V vs Hg/HgO in the positive-going scan, and the reduction of β-NiOOH species to β-$Ni(OH)_2$ occurs between +0.50 and +0.20 V in the negative-going scan. For potential higher than +0.60 V in the positive-going scan, the increase of current density is related to the oxygen evolution reaction. At last, a reduction process in the −0.15 to −0.35 V vs Hg/HgO, identified by the navy rectangle in Figure 5a, is the reduction of either another nickel oxide species or of oxygen generated during the oxygen evolution reaction (OER).[52]

In the case of data normalization for Ni_xM_{1-x}/C materials, it is complex to evaluate the electroactive surface areas (EASA) with the use of a bimetallic as the estimation involves many uncertainties.[53] Therefore, the currents were normalized with geometric surface area of the GC disk (0.071 cm^{-2}). Upon comparison of the CVs in Figure 5, the different Ni_xM_{1-x}/C catalysts clearly exhibit separate potential regions for the surface reactions of their respective cocatalysts (Pd, Au, and Bi). For $Ni_{80}Pd_{20}/C$, the small cathodic peak appearing at −0.36 V vs Hg/HgO is attributed to the reduction of Pd oxides (PdO).[1,20] The cathodic peak close to +0.14 vs Hg/HgO for $Ni_{90}Au_{10}/C$ is associated with the reduction of the quasi-2D oxide state of Au (AuO or $Au(OH)_2$).[1,54] Whereas for $Ni_{90}Bi_{10}/C$, an anodic peak appears at lower potential (∼−0.52 V vs Hg/HgO), which corresponds to a thin layer formation of $Bi(OH)_3$ sites at the electrode surface.[36]

By comparing CVs in the presence and the absence of glycerol, we observe that the onset potential of GEOR is shifted toward lower potential by as much as ∼180 to 370 mV less than the potential for the $Ni^{II} \rightarrow Ni^{III}$ transition (Figure 5b and Figure S15). This phenomenon is attributed to the dependency of GEOR with the preliminary steps of the transformation of β-$Ni(OH)_2$ into β-NiOOH. A similar observation was already detected by Oliveria et al. and Houache et al.[22−24,20]

The LSVs of GEOR in 1.0 M KOH + 0.1 M glycerol were recorded at 0.05 and 0.001 V s^{-1}, respectively, on the different Ni-rich catalysts (Figure 6 and Figure S16). The Ni/C catalyst presents an onset potential for GEOR close to 0.31 V vs Hg/HgO, which is approximately 100, 180, and 140 mV lower than our previous studies on unsupported Ni[37] and bulk Ni, before and after treatment in ascorbic acid, respectively.[20]

https://dx.doi.org/10.1021/acsaem.0c01282
ACS Appl. Energy Mater. 2020, 3, 8725−8738

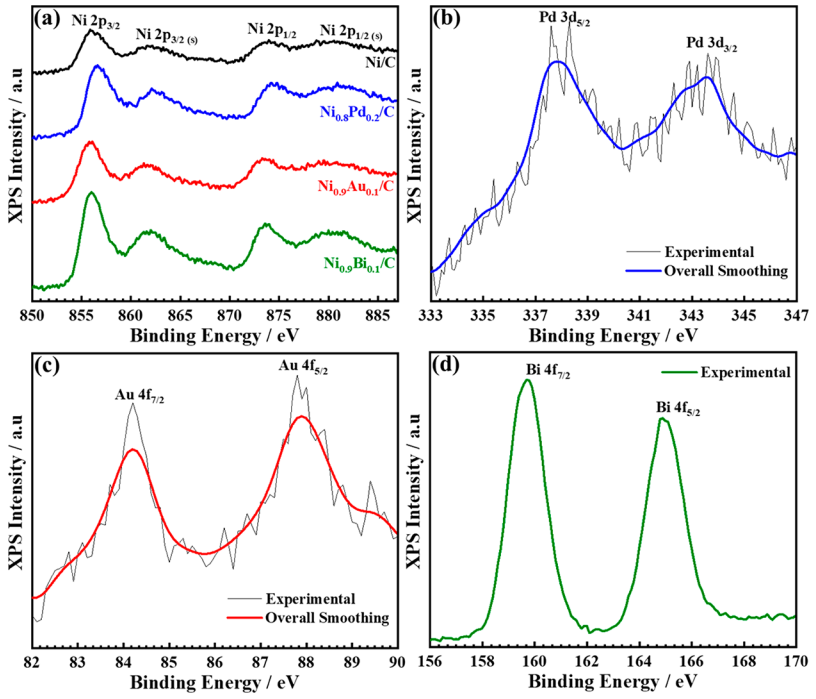

Figure 4. High-resolution XPS spectra of Ni_xM_{1-x}/C (M = Pd, Au, and Bi) corresponding to (a) Ni 2p, (b) Pd 3d in $Ni_{0.8}Pd_{0.2}/C$, (c) Au 4f in $Ni_{0.9}Au_{0.1}/C$, and (d) Bi 4f in $Ni_{0.9}Bi_{0.1}/C$.

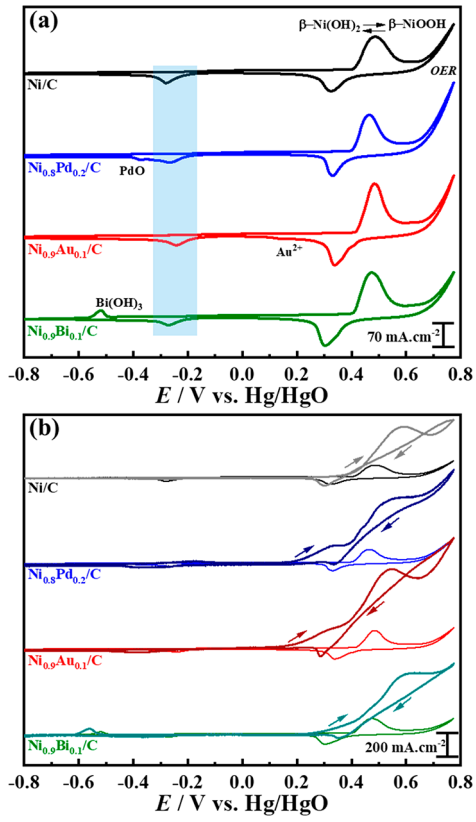

Figure 5. Cyclic voltammograms of Ni_xM_{1-x}/C (M = Pd, Au, and Bi) catalysts in N_2-purged (a) 1.0 M KOH and (b) 1.0 M KOH + 0.10 M glycerol electrolyte (bold line) at 0.05 V s^{-1} scan rate and 293 K (fifth stable cycle).

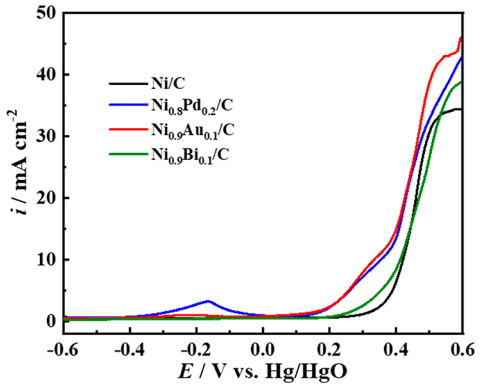

Figure 6. LSVs of Ni_xM_{1-x}/C (M = Pd, Au, and Bi) catalysts in N_2-purged 1.0 M KOH + 0.1 M glycerol electrolyte at 0.001 V s^{-1} scan rate and 293 K.

In comparison, bimetallic Ni_xM_{1-x}/C materials present a shift of the onset potential toward lower values for glycerol electro-oxidation than that of monometallic. Among different materials, the $Ni_{0.9}Au_{0.1}/C$ electrocatalyst displayed the highest current density, reaching 46 mA cm^{-2} with a concurrent onset potential at ∼+0.12 V vs Hg/HgO. In contrast, the $Ni_{0.8}Pd_{0.2}/C$ catalyst has slightly higher onset potential (E_{onset} = ∼+0.16 V vs Hg/HgO) compared to Ni_xAu_{1-x}/C (Figure S16a). An additional oxidation peak appears at ca. ∼−0.35 V vs Hg/HgO ascribed to GEOR on Pd sites, indicating that palladium by itself has significantly lower onset potentials compared to nickel.[20] Figure S16b illustrates that only higher Pd content of 20 at. % was able to observe this oxidation peak which could be due to two possible reasons: (i) the presence of a rich Ni causes some surface segregation of the Pd active sites as shown in EELS mapping (Figure 3a), and (ii) excess formation of Ni^{2+} increases the concentration of OH_{ads} and/or OH^-, which in turn could hamper glycerol transportation to the Pd active sites.[53] Moreover, the onset potential of GEOR on the $Ni_{0.98}Bi_{0.02}/C$ and $Ni_{0.95}Bi_{0.05}/C$ materials was approximately

https://dx.doi.org/10.1021/acsaem.0c01282
ACS Appl. Energy Mater. 2020, 3, 8725−8738

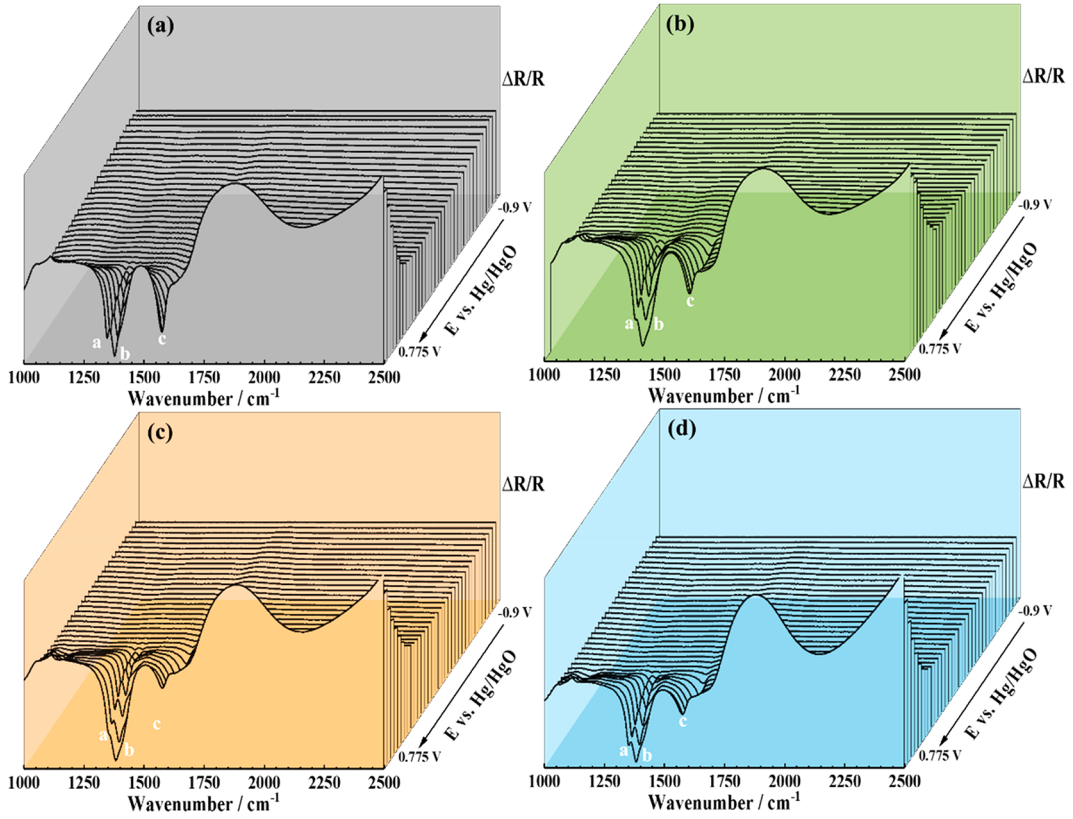

Figure 7. Infrared spectra recorded during GEOR on (a) Ni/C, (b) $Ni_{0.8}Pd_{0.2}$/C, (c) $Ni_{0.9}Au_{0.1}$/C, and (d) $Ni_{0.9}Bi_{0.1}$/C catalysts in 1.0 M KOH + 0.1 M glycerol electrolyte at 293 K. Scan rate: 0.001 V s^{-1}, resolution 4 cm^{-1}.

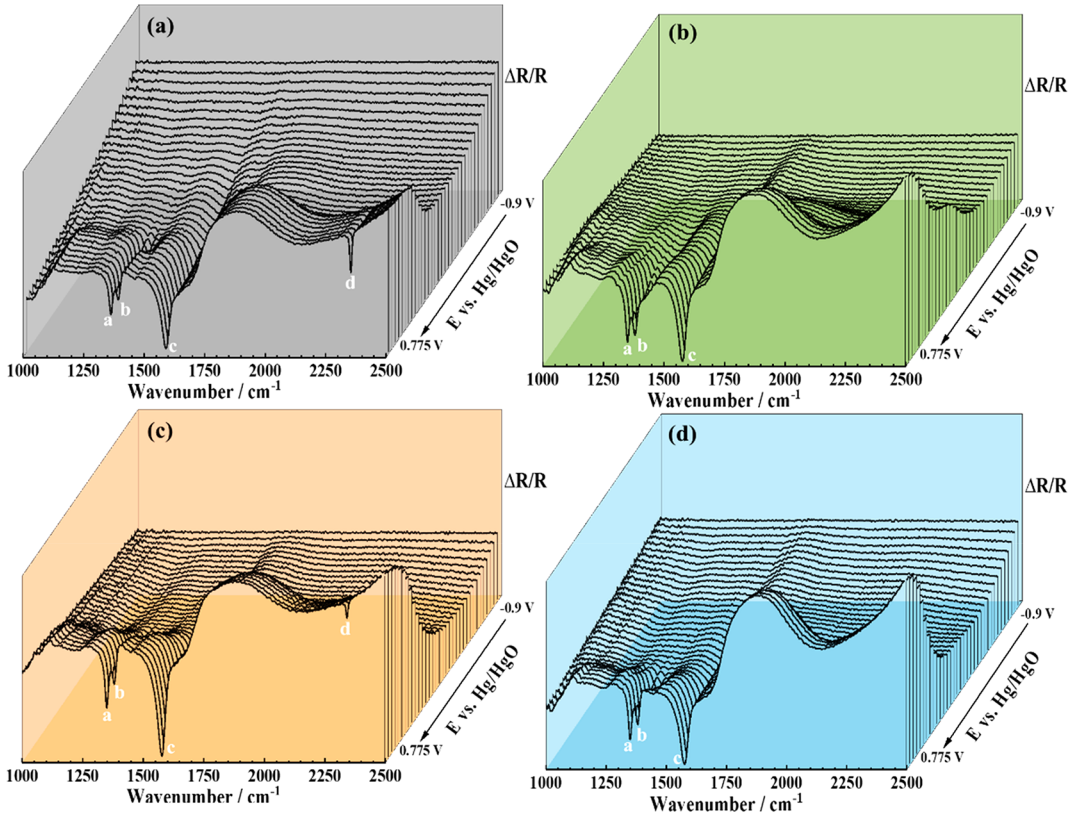

Figure 8. Infrared spectra recorded during GEOR on (a) Ni/C, (b) $Ni_{0.8}Pd_{0.2}$/C, (c) $Ni_{0.9}Au_{0.1}$/C, and (d) $Ni_{0.9}Bi_{0.1}$/C catalysts in 0.1 M KOH + 0.1 M glycerol electrolyte at 293 K. Scan rate: 0.001 V s^{-1}, resolution 4 cm^{-1}.

https://dx.doi.org/10.1021/acsaem.0c01282
ACS Appl. Energy Mater. 2020, 3, 8725−8738

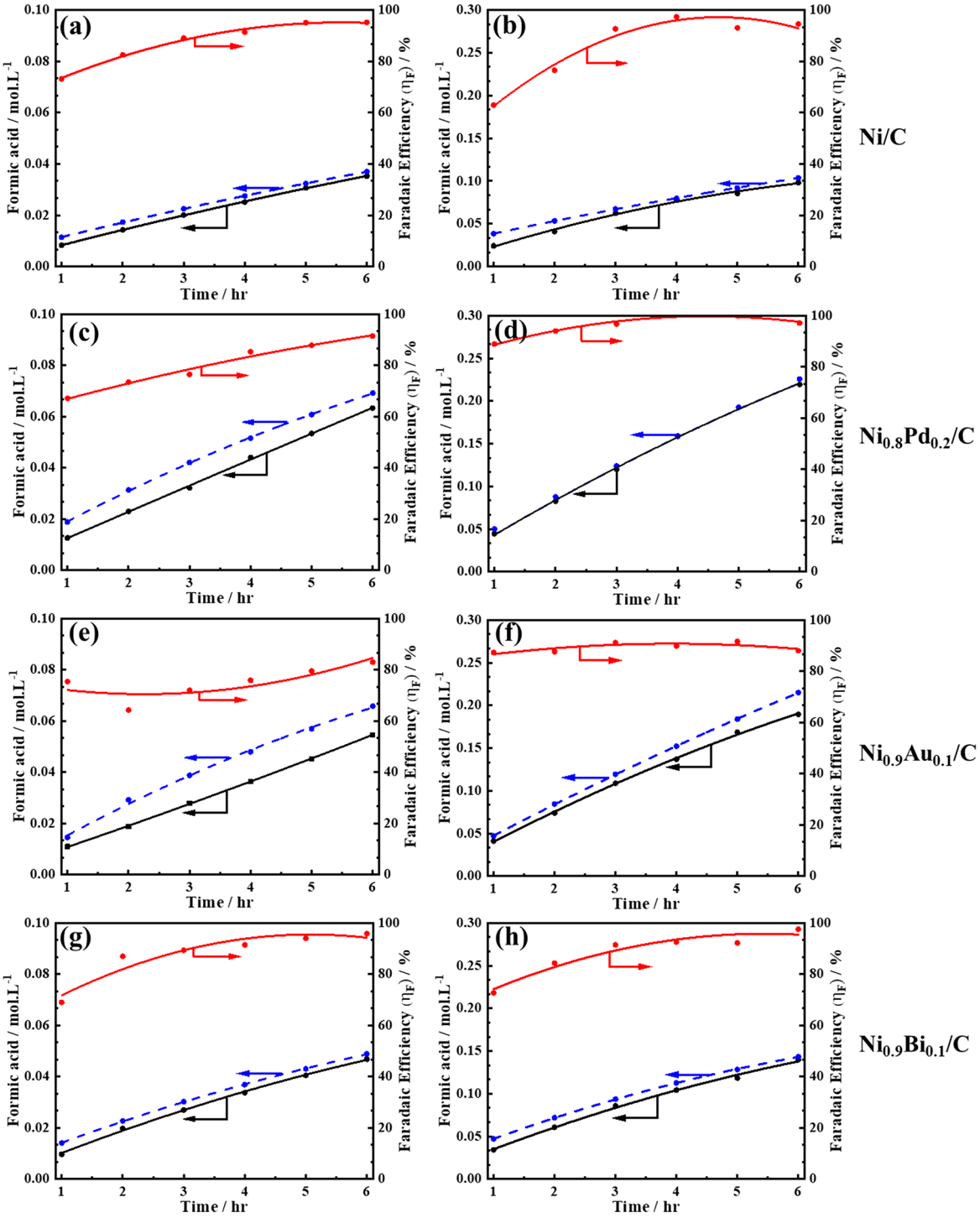

Figure 9. Comparison of the experimental concentration of formate determined by HPLC (black line) with the theoretical one for a 100% selectivity (blue dotted line) and Faradaic efficiency for formate production (red line) as a function of electrolysis time on (a, b) Ni/C, (c, d) $Ni_{0.8}Pd_{0.2}/C$, (e, f) $Ni_{0.9}Au_{0.1}/C$, and (g, h) $Ni_{0.9}Bi_{0.1}/C$ at +1.30 V (on the left-hand side) and +1.55 V (on the right-hand side).

the same as that on Ni/C, with the maximum current density slightly higher in $Ni_{0.95}Bi_{0.05}/C$ (Figure S16c). However, at high bismuth content of 10 at. % the overpotential dropped by 0.08 V compared to Ni/C.

In summary, small addition (≤20 at. %) of Pd, Au, or Bi atoms to Ni nanoparticles clearly indicates that GEOR on the bimetallic catalysts improves the activity and significantly shifts the onset potential to lower values. This enhancement could be attributed to the changes in the electronic interactions between the active sites and the reactant on the catalysts, thereby altering d-band center of the metals. The relative d-band center is closely associated with the molecule's adsorption, thus varying the catalytic activity.[55]

3.3. *In Situ* Infrared Spectroscopy Measurements. The *in situ* spectroelectrochemical measurements have been performed to shed light on the GEOR process, taking place at the electrolyte/electrode interface on 10 different Ni-rich catalysts. Infrared spectra were recorded as a function of the

https://dx.doi.org/10.1021/acsaem.0c01282
ACS Appl. Energy Mater. 2020, 3, 8725−8738

electrode potential in a N_2-purged 1.0 and 0.1 M KOH electrolyte at 293 K and 0.001 V s^{-1} for the electro-oxidation of 0.1 M glycerol as shown in Figures 7−8 and Figures S17−S18. Spectra recorded for GEOR in high KOH concentration (1.0 M) lead to the formation of three main absorption peaks in the so-called infrared fingerprint region of the organic molecules between 1100 and 1600 cm^{-1}, labeled as bands A to C in each figure (Figure 7 and Figure S17). These three peaks occur instantaneously at around 1350, 1385, and 1581 cm^{-1} (bands A, B, and C in Figure 7 and Figure S17). The absorption band at ∼1350 cm^{-1} corresponds to symmetric (O−C−O) stretching of formate.[56] The band located at ∼1385 cm^{-1} is clearly associated with symmetric (O−C−O) stretching of formate and glycerate.[37,56] Besides, the absorption peak detected at 1581 cm^{-1} is assigned to a different asymmetric COO^- group of carboxylate species[22−24] with a shoulder at ∼1670 cm^{-1}. These three absorption peaks appear on all the materials with different intensities, demonstrating that the main reaction products do not alter depending on the catalyst composition and applied potential considered in this study. In the context of variation of absorption band intensities, functional groups are consumed or formed at different rates. Upward absorption peaks at ∼1050 and 1113 cm^{-1} assigned to ν(C−O) stretching of CH_2−OH functions correspond to glycerol consumption.[57]

Similar remarks for lower concentration KOH (0.1 M) can be made from the infrared spectra recorded for glycerol electro-oxidation on the different Ni-rich catalysts (Figure 8 and Figure S18). The absorption peaks are positioned at the same wavenumber values as for higher KOH concentration (1 M KOH), indicating a similar formation of the functional species stated above. An intense peak appears at 2343 cm^{-1} on Ni/C for E > +0.53 V vs Hg/HgO (band D in Figure 8a), which has lower intensity on Ni_xAu_{1-x}/C materials at E = 0.775 V vs Hg/HgO (Figure 8c and Figure S18c,d). This absorption peak corresponds to CO_2 formation.[22,23]

In those cases, it is worth noting the presence of an absorption band between 1400 and 1450 cm^{-1}, which could be attributed to the formation of carbonates. However, the CO_2 absorption band is not visible with Ni_xPd_{1-x}/C (Figure 8b and Figure S18a,b) and Ni_xBi_{1-x}/C (Figure 8d and Figure S18e,f) materials as well as the absorption bands between 1400 and 1450 cm^{-1}. The same observation can be made for all catalysts tested in 1.0 M KOH: the increase of the KOH concentration avoids the formation of carbonate and CO_2 and favors the formation of formate. The CO_2 visibility is mainly due to the change of interfacial pH to acid due to the consumption of hydroxyl in a thin layer close to electrode and CaF_2 prism.[20,22−24]

From both these studies, all Ni_xM_{1-x}/C catalysts are very promising in terms of activity and selectivity toward formate formation at mild electrode potentials and high KOH concentration. For this reason, Ni/C, $Ni_{0.8}Pd_{0.2}$/C, $Ni_{0.9}Au_{0.1}$/C, and $Ni_{0.9}Bi_{0.1}$/C catalysts were selected to perform continuous scale-up electrolysis measurements for 24 h to accumulate reaction products and determine the selectivity of glycerol electro-oxidation in 1.0 M KOH.

3.4. Electrolysis Measurements. The mechanistic analysis was accomplished to determine the reaction products by HPLC and NMR after applying CA measurements in a 25 cm^2 (geometric area) continuous electrolysis cell for 24 h at two constant cell voltages of +1.30 and +1.55 V selected from the *in situ* infrared study. For GEOR at the anodic compartment, the current dropped monotonically over the 24 h electrolysis time range as shown in Figure S19.

The analyses by HPLC of the reaction mixture were performed every hour for 6 h using an aliquot of 0.6 mL of solution. The data (Figure S20a−d) show the evolution of the chromatograms with the time of glycerol electrolysis on Ni/C, $Ni_{0.8}Pd_{0.2}$/C, $Ni_{0.9}Au_{0.1}$/C, and $Ni_{0.9}Bi_{0.1}$/C catalysts. In all figures, the main peak is detected at retention time of ∼10.46 min for GEOR, clearly corresponding to formic acid which is confirmed by the reference chromatogram (Figure S21a). Hence, at +1.30 V two additional small peaks appear at retention time of ∼8.31 and 9.45 min. The first peak (at ∼8.31 min) appears after 1 h electrolysis and remains stagnant for a longer period; this could be due to the injection peak or the formation of glyceric acid in a negligible quantity at the very early stage of electrolysis measurements. The second peak (∼9.45 min) increases gradually with time and is mainly pronounced for the $Ni_{0.9}Au_{0.1}$/C catalyst. We propose that it could be the formation of lactic acid in small traces, since this compound is well-known to be selective toward GEOR on gold materials.[58] These two peaks were confirmed by the reference chromatogram as shown in Figure S21b,c. While at higher cell voltage (U_{cell} = +1.55 V), only the formate peak was evident.

Figures 9a−h compare the experimental concentration of formate ($C_{formate,exp}$) performed by HPLC experiments with the theoretical concentration of formate ($C_{formate,theo}$) determined by Faraday's law via eight-electron process, assuming only the formation of formate as shown in reaction 2:

$$C_3H_8O_3 + 11OH^- \rightarrow 3CHO_2^- + 8H_2O + 8e^- \quad (2)$$

Finding the resulting Faradaic efficiency for formate formation can be given by using eq 3:[1]

$$\eta_F = \frac{C_{formate,exp}}{C_{formate,theo}} \quad (3)$$

First, in the case of Ni/C and $Ni_{0.9}Bi_{0.1}$, a very good agreement between the experimental concentration of formate determined by HPLC and the theoretical one for a 100% selectivity is obtained for both cell voltages, the difference lying certainly in the standard deviations of the experiment. This observation indicates a very selective production of formate with these catalysts. The curves at low cell voltage (U_{cell} = +1.30 V) for $Ni_{0.8}Pd_{0.2}$/C and $Ni_{0.9}Au_{0.1}$/C in Figures 9c and 9e, respectively, do not overlap, demonstrating that other products are generated. It can be reasonably proposed that the supplementary product corresponds to that detected at 9.45 min by HPL. It seems that this product acts as intermediate which is not stable in GEOR and tends to be further oxidized to formate at high cell voltage (+1.55 V), as both curves become closer each other (Figure 9d,f).

Because of these limit scenarios, it was possible to calculate the limit concentration of glycerol ($C^{8e-}_{Glycerol}(t)$) and its conversion ($X^{8e-}_{Glycerol}(t)$) at different reaction times assuming 100% selectivity to formate, according to the following equations:

$$C_{Glycerol}(t) = 0.1 - \frac{C_{formate,exp}(t)}{3} \quad (4)$$

$$X_{Glycerol}(t) = \frac{0.1 - C_{glycerol}(t)}{0.1} \quad (5)$$

https://dx.doi.org/10.1021/acsaem.0c01282
ACS Appl. Energy Mater. 2020, 3, 8725−8738

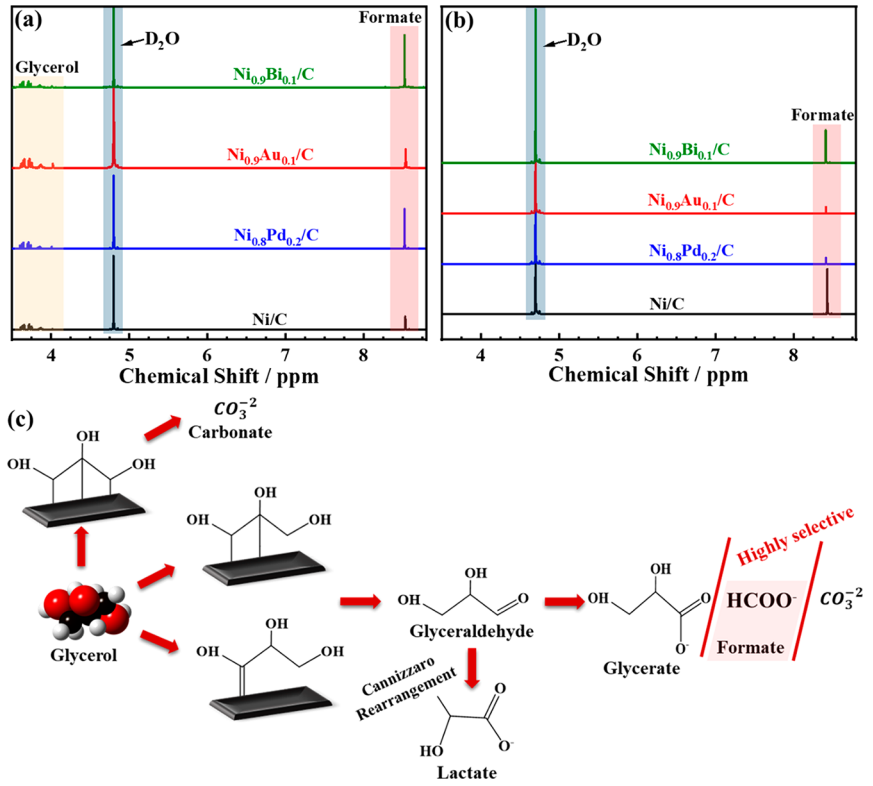

Figure 10. ^{1}H NMR spectra of 1.0 M KOH + 0.1 M glycerol solution after neutralization with HCl, lyophilization, and dissolution into D_2O. The spectra correspond to different Ni-based catalysts at the cell voltages of (a) +1.30 V and (b) +1.55 V after 24 h of electrolysis. (c) Suggested reaction pathways for GEOR over Ni_xM_{1-x}/C (M = Pd, Au, and Bi) catalysts.

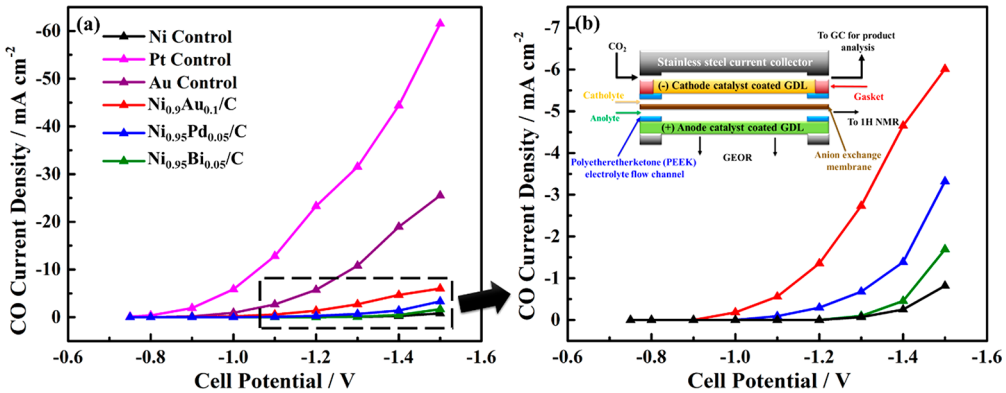

Figure 11. (a) Coelectrolysis performance of the most active carbon supported NiAu, NiPd, and NiBi nanocatalysts as well as the Pt, Au, and Ni/C controls. The graph plots the partial CO current density with respect to applied cell potential; the graph on the right (b) magnifies the data from Ni-based anodes with a schematic representation of the setup.

All obtained results are summarized in Table S2. For 6 h electrolysis of glycerol on Ni/C, the conversion rates increase significantly by applying higher applied potentials, i.e., 11.7% and 32.7% for U_{cell} = +1.30 and +1.55 V, respectively. Compared to Ni/C, the bimetallic catalysts show a better tendency for glycerol conversion throughout the electrolysis duration. $Ni_{0.8}Pd_{0.2}/C$ and $Ni_{0.9}Au_{0.1}/C$ have the highest value after 6 h electrolysis with glycerol conversion of 73.1% and 63.1%, respectively. In the case of $Ni_{0.9}Bi_{0.1}/C$ catalyst, the results are still impressionable, with 46.4% conversion and 100% selectivity toward formate.

At the end of the electrolysis measurements an additional identification technique (^{1}H NMR) was performed to identify the product distribution after 24 h of CA in 0.1 M glycerol solution (Figure 10a,b). The ^{1}H NMR spectra of the initial solution (1.0 M KOH + 0.1 M glycerol) before electrolysis measurement (Figure S22a,b) exhibit typical signals for glycerol with several peaks in the 3.4−3.7 ppm range and a standard solution (1.0 M KOH + 0.1 M formate) with a single formate peak at ∼8.4 ppm. After 24 h electrolysis at a cell voltage of +1.30 V, the signal of glycerol has been reduced for all catalysts as shown in Figure 10a, while at higher voltage (U_{cell} = +1.55 V), the glycerol peaks disappear completely, indicating 100% conversion (Figure 10b). Furthermore, in ^{1}H NMR spectra formate has been detected as the major product ($\delta \approx 8.4$ ppm), which indicates that the C−C bond of glycerol was broken. In addition, it is noteworthy to mention that the intensity of the formate signal at +1.55 V decreases for all

https://dx.doi.org/10.1021/acsaem.0c01282
ACS Appl. Energy Mater. 2020, 3, 8725−8738

$Ni_{1-x}M_x/C$ compared to that at +1.30 V. This translates likely in the higher ability of modified Ni catalysts for the formation of CO_3^{2-}.

In summary, all qualification and quantification analyses are in good correlation, indicating the formation of formate as one of the major products on the anode carbon supported Ni−M shell−core structures with cathodic hydrogen production; we suggested the reaction mechanism in Figure 10c. The counter electrode reaction on Pt/C hydrogen at a cell voltage as low as +1.30 V corresponds to the low energy consumption of ∼35 kWh kg^{-1}.[59]

3.5. Coelectrolysis of CO_2 and Glycerol in a Flow Electrolyzer. A possible approach to achieve cost-effective electro-oxidation of glycerol using Ni-rich bimetallic catalysts is to execute this reaction parallel with CO_2 electroreduction using Ag NPs as cathode catalyst. Running this coelectrolysis process in a flow electrolyzer revealed that all Ni bimetallic catalysts are active toward GEOR, as shown in Figure 11 and Figures S23−S25. Out of all the Ni_xAu_{1-x}/C catalysts, the $Ni_{0.9}Au_{0.1}/C$ catalyst achieved the highest partial CO current density of ∼6.0 mA cm^{-2} at −1.5 V, as shown in Figure S24. For the Ni_xPd_{1-x}/C and Ni_xBi_{1-x}/C samples, the best performers were $Ni_{0.95}Pd_{0.05}/C$ and $Ni_{0.95}Bi_{0.05}/C$, showing partial CO current densities of about 3.3 and 1.7 mA cm^{-2}, respectively, at 1.5 V (Figures S23 and S25). Adding Au and Pd to Ni enhances the activity; however, Bi behaves similarly to Ni as both the Ni_xBi_{1-x}/C and Ni/C anodes depicted the lowest activities. Compared to the carbon-supported $Ni_{0.95}Bi_{0.05}$ and Ni, both $Ni_{0.9}Au_{0.1}/C$ and $Ni_{0.95}Pd_{0.05}/C$ anodes exhibit lower onset cell voltages for the CO_2 electroreduction. The onset cell potential value for Ni/C and $Ni_{0.95}Bi_{0.05}/C$ is around −1.30 V, while using $Ni_{0.9}Au_{0.1}/C$ and $Ni_{0.95}Pd_{0.05}/C$ dropped the cell voltage significantly by 0.3 V ($U_{cell,onset}$ = −1.0 V) and 0.2 V ($U_{cell,onset}$ = −1.1 V), respectively, as illustrated in Figure 11b. We also noticed in Figure 11a that both reference Pt and Au monometallic catalysts at the anode outperform all of the Ni-rich bimetallic catalysts, leading to better overall activity (62 and 25 mA cm^{-2} at −1.5 V, respectively) with lower onset cell potentials (E_{onset} = −0.75 and −0.9 V, respectively) for CO_2 electroreduction. Furthermore, ^{1}H NMR analysis of the anolyte indicates the formation of both formate and lactate in this coelectrolysis experiment as illustrated in Figure S26.

If we were to attempt a durability study with these catalysts, we would continuously apply 1.5 V and monitor any the total current and CO Faradaic efficiency for changes. However, because the total current for all Ni_xAu_{1-x}/C experiments at this cell potential was <10 mA cm^{-2}, the durability test would not provide much insight into catalyst stability because it is a relatively low current compared to the capabilities of the flow cell and industrially relevant current densities (≥200 mA cm^{-2}).[60−62] Increasing the cell potential would indeed provide higher current densities but would also begin to introduce OER and therefore negate the study of GEOR for these catalysts.

With these active anodes, the entire flow electrolyzer requires less cell voltage (total energy) to reduce CO_2 to CO, an observation we also noted in our previous work when using Pt at the anode.[13] Reducing the total energy helps to make all electroreduction products more feasible by widening the operating cell potential range.[61] Lowering the energy requirement of coelectrolysis also reduces carbon emissions considering the supplying electrical grid is only partially renewable.[13] As stated earlier, Pt and Au are more active for CO_2 electroreduction; however, these catalysts are precious metals and thus drive up the cost for the capital expenditure of this electrolysis setup. Specifically, the market prices of Pt, Au, and Ni are approximately 30, 52, and 0.016 USD g^{-1}, respectively.[63−65] Ultimately, being able to utilize Ni as the main component of the anode catalysts could reduce the catalyst price significantly (∼2000−3000 lower). This saving reduces the cost of the setup and in turn decreases the minimum current density needed to make production of CO_2 electroreduction commodities (CO in our case) more feasible.[61]

4. CONCLUSION

Nanosized materials based on nickel-rich metals have been prepared by a heatless coreduction method. The Ni_xM_{1-x}/C (M = Bi, Pd, and Au) nanocatalysts with different atomic ratios (≤20%) have been characterized, indicating the possibility of a M-core Ni-shell structure which optimized the performance of these materials. The electrochemical measurements performed in 1.0 M KOH electrolyte permitted the surface characterization of each electrode catalyst. As evidenced, the Pd, Au, and Bi elements were present in their composition, and they modified the electronic properties of Ni to shift the overpotential to lower values, by as much as 0.19 to 0.08 V for GEOR. *In situ* infrared spectroscopy measurements showed that the major product was formate, which is attributed to symmetric and asymmetric carboxylate species. However, no significant change in selectivity was observed for all Ni_xM_{1-x}/C. In addition to Ni/C, we chose the three best catalysts to run 24 h continuous electrolysis in a 25 cm^2 cell at a potential of +1.30 and +1.55 V, and the reaction products were analyzed by HPLC and ^{1}H NMR. After 1 h electrolysis, both applied potentials led to 100% selectivity for formate production, which is in a good correlation with a qualitative analysis. At higher voltage (U_{cell} = +1.55 V), the glycerol peaks disappear completely, indicating 100% conversion after 24 h electrolysis for all four catalysts. Moreover, cogeneration of value-added products at the anode using cost-effective Ni_xM_{1-x}/C in combination with CO_2 electroreduction to CO at the cathode using Ag was tested. These flow electrolyzer experiments revealed that, out of all Ni_xM_{1-x}/C catalysts, the $Ni_{0.9}Au_{0.1}/C$ catalyst achieved the highest partial current density for CO of ∼6.0 mA cm^{-2} and lowest onset cell voltage of −1.0 V, which are in good agreement with the electrochemical measurements. All these insights anticipate the possibility to control the selectivity and activity of these Ni-based electrocatalysts toward a given product.

■ ASSOCIATED CONTENT

Supporting Information

The Supporting Information is available free of charge at https://pubs.acs.org/doi/10.1021/acsaem.0c01282.

Physiochemical characterization of Ni_xM_{1-x} (M = Pd, Au, and Bi), including XRD, TGA, SAED, STEM images, O 1s XPS, EDS mapping, EDS, and EELS spectra; remaining electrochemical measurements normalized with geometric surface area, FTIR spectra with CA profile for electrolysis, product distributions (HPLC and ^{1}H NMR) at different applied potentials for different reaction times along with chromatograms of the standards; coelectrolysis performance and product

https://dx.doi.org/10.1021/acsaem.0c01282
ACS Appl. Energy Mater. 2020, 3, 8725−8738

distribution of Ni_xM_{1-x} (M = Pd, Au, and Bi) at the anode with CO_2 electroreduction (PDF)

AUTHOR INFORMATION

Corresponding Author

Elena A. Baranova − *Department of Chemical and Biological Engineering, Centre for Catalysis Research and Innovation, University of Ottawa, Ottawa, ON K1N 6N5, Canada;* orcid.org/0000-0001-5993-2740; Phone: 16135625800; Email: elena.baranova@uottawa.ca; Fax: 16135625172

Authors

Mohamed S. E. Houache − *Department of Chemical and Biological Engineering, Centre for Catalysis Research and Innovation, University of Ottawa, Ottawa, ON K1N 6N5, Canada;* orcid.org/0000-0002-3944-9660

Reza Safari − *Department of Materials Science and Engineering, McMaster University, Hamilton, ON L9H 4L7, Canada*

Uzoma O. Nwabara − *Department of Chemical and Biomolecular Engineering, University of Illinois at Urbana−Champaign, Urbana, Illinois 61820, United States; International Institute for Carbon Neutral Energy Research (WPI-I2CNER), Kyushu University, Fukuoka, Japan*

Thibault Rafaïdeen − *IC2MP, UMR CNRS, Université de Poitiers, 86073 Cedex 9 Poitiers, France*

Gianluigi A. Botton − *Department of Materials Science and Engineering, McMaster University, Hamilton, ON L9H 4L7, Canada;* orcid.org/0000-0002-8746-1146

Paul J. A. Kenis − *Department of Chemical and Biomolecular Engineering, University of Illinois at Urbana−Champaign, Urbana, Illinois 61820, United States; International Institute for Carbon Neutral Energy Research (WPI-I2CNER), Kyushu University, Fukuoka, Japan;* orcid.org/0000-0001-7348-0381

Stève Baranton − *IC2MP, UMR CNRS, Université de Poitiers, 86073 Cedex 9 Poitiers, France*

Christophe Coutanceau − *IC2MP, UMR CNRS, Université de Poitiers, 86073 Cedex 9 Poitiers, France;* orcid.org/0000-0001-5464-7721

Complete contact information is available at: https://pubs.acs.org/10.1021/acsaem.0c01282

Notes

The authors declare no competing financial interest.

ACKNOWLEDGMENTS

The authors acknowledge Ni Electro Can project administered from Queen's University and supported by Grant RGPNM 477963-2015 under the Natural Sciences and Engineering Research Council of Canada (NSERC) Discovery Frontiers Program. The support by Mitacs Globalink Research Award Abroad (Application Ref. IT 10871) is also acknowledged for travel funds to Université de Poitiers. Part of the electron microscopy work was performed at the Canadian Centre for Electron Microscopy, a national facility supported by the Canada Foundation for Innovation under the Major Science Initiative program, NSERC, and McMaster University. We are grateful to Canmet Materials Technology Laboratory (Hamilton, Ontario) for access to the Osiris STEM for energy dispersive spectroscopy work and Andreas Korinek (from CCEM) for carrying out some of the measurements. XPS was performed in the Frederick Seitz Materials Research Laboratory Central Research Facilities, University of Illinois.

REFERENCES

(1) Rafaïdeen, T.; Baranton, S.; Coutanceau, C. Highly efficient and selective electrooxidation of glucose and xylose in alkaline medium at carbon supported alloyed PdAu nanocatalysts. *Appl. Catal., B* **2019**, *243*, 641−656.

(2) Dodekatos, G.; Schünemann, S.; Tüysüz, H. Recent advances in thermo-, photo-, and electrocatalytic glycerol oxidation. *ACS Catal.* **2018**, *8*, 6301−6333.

(3) Coutanceau, C.; Baranton, S. Electrochemical conversion of alcohols for hydrogen production: a short overview. *Wiley Interdisciplinary Reviews: Energy and Environment* **2016**, *5*, 388−400.

(4) Lam, C. H.; Bloomfield, A. J.; Anastas, P. T. A switchable route to valuable commodity chemicals from glycerol via electrocatalytic oxidation with an earth abundant metal oxidation catalyst. *Green Chem.* **2017**, *19*, 1958−1968.

(5) Holade, Y.; Servat, K.; Tingry, S.; Napporn, T. W.; Remita, H.; Cornu, D.; Kokoh, K. B. Advances in electrocatalysis for energy conversion and synthesis of organic molecules. *ChemPhysChem* **2017**, *18*, 2573−2605.

(6) Zhang, Z.; Xin, L.; Qi, J.; Chadderdon, D. J.; Sun, K.; Warsko, K. M.; Li, W. Selective electro-oxidation of glycerol to tartronate or mesoxalate on Au nanoparticle catalyst via electrode potential tuning in anion-exchange membrane electro-catalytic flow reactor. *Appl. Catal., B* **2014**, *147*, 871−878.

(7) Houache, M. S. E.; Hughes, K.; Baranova, E. A. Study on catalyst selection for electrochemical valorization of glycerol. *Sus. Energy Fuels* **2019**, *3*, 1892−1915.

(8) Coutanceau, C.; Zalineeva, A.; Baranton, S.; Simoes, M. Modification of palladium surfaces by bismuth adatoms or clusters: Effect on electrochemical activity and selectivity towards polyol electrooxidation. *Int. J. Hydrogen Energy* **2014**, *39*, 15877−15886.

(9) Simões, M.; Baranton, S.; Coutanceau, C. Electrochemical valorisation of glycerol. *ChemSusChem* **2012**, *5*, 2106−2124.

(10) Baranton, S.; Coutanceau, C. Nickel cobalt hydroxide nanoflakes as catalysts for the hydrogen evolution reaction. *Appl. Catal., B* **2013**, *136*, 1−8.

(11) Marozzi, C. A.; Chialvo, A. C. Development of electrode morphologies of interest in electrocatalysis. Part 1: Electrodeposited porous nickel electrodes. *Electrochim. Acta* **2000**, *45*, 2111−2120.

(12) Marozzi, C. A.; Chialvo, A. C. Development of electrode morphologies of interest in electrocatalysis: part 2: hydrogen evolution reaction on macroporous nickel electrodes. *Electrochim. Acta* **2001**, *46*, 861−866.

(13) Verma, S.; Lu, S.; Kenis, P. J. Co-electrolysis of CO_2 and glycerol as a pathway to carbon chemicals with improved technoeconomics due to low electricity consumption. *Nature Energy* **2019**, *4*, 466.

(14) Castagna, R. M.; Sieben, J. M.; Alvarez, A. E.; Duarte, M. M. Electrooxidation of ethanol and glycerol on carbon supported PtCu nanoparticles. *Int. J. Hydrogen Energy* **2019**, *44*, 5970−5982.

(15) State of the States. Fuel Cells in America 2016, 7th ed.; Fuel Cell Technologies Office, U.S. Department of Energy (DOE): 2016; https://www.energy.gov/sites/prod/files/2016/11/f34/fcto_state_of_states_2016_0.pdf (accessed on January 2020).

(16) Faro, M. L.; Minutoli, M.; Monforte, G.; Antonucci, V.; Aricò, A. S. Glycerol oxidation in solid oxide fuel cells based on a Ni-perovskite electrocatalyst. *Biomass Bioenergy* **2011**, *35*, 1075−1084.

(17) Freitas, M. B. J. G. Nickel hydroxide powder for NiO· OH/Ni $(OH)_2$ electrodes of the alkaline batteries. *J. Power Sources* **2001**, *93*, 163−173.

(18) Tehrani, R. M.; Ab Ghani, S. Electrocatalysis of free glycerol at a nanonickel modified graphite electrode and its determination in biodiesel. *Electrochim. Acta* **2012**, *70*, 153−157.

(19) Nam, K. W.; Yoon, W. S.; Kim, K. B. X-ray absorption spectroscopy studies of nickel oxide thin film electrodes for supercapacitors. *Electrochim. Acta* **2002**, *47*, 3201−3209.

(20) Houache, M. S. E.; Cossar, E.; Ntais, S.; Baranova, E. A. Electrochemical modification of nickel surfaces for efficient glycerol electrooxidation. *J. Power Sources* **2018**, *375*, 310−319.
(21) Allagui, A.; Sarfraz, S.; Baranova, E. A. Ni_xPd_{1-x} (x= 0.98, 0.93, and 0.58) nanostructured catalysts for ammonia electrooxidation in alkaline media. *Electrochim. Acta* **2013**, *110*, 253−259.
(22) Oliveira, V. L.; Morais, C.; Servat, K.; Napporn, T. W.; Tremiliosi-Filho, G.; Kokoh, K. B. Studies of the reaction products resulted from glycerol electrooxidation on Ni-based materials in alkaline medium. *Electrochim. Acta* **2014**, *117*, 255−262.
(23) Oliveira, V. L.; Morais, C.; Servat, K.; Napporn, T. W.; Tremiliosi-Filho, G.; Kokoh, K. B. Glycerol oxidation on nickel based nanocatalysts in alkaline medium−Identification of the reaction products. *J. Electroanal. Chem.* **2013**, *703*, 56−62.
(24) Oliveira, V. L.; Morais, C.; Servat, K.; Napporn, T. W.; Olivi, P.; Kokoh, K. B.; Tremiliosi-Filho, G. Kinetic investigations of glycerol oxidation reaction on Ni/C. *Electrocatalysis* **2015**, *6*, 447−454.
(25) Du, J.; Xie, A.; Zhu, S.; Xiong, Z.; Yu, X.; Yang, F.; Tao, Y.; Luo, S. 3D flower-like CoNi 2 S 4/polyaniline with high performance for glycerol electrooxidation in an alkaline medium. *New J. Chem.* **2019**, *43*, 10366−10375.
(26) Liu, Z.; Li, Z.; Wang, F.; Liu, J.; Ji, J.; Wang, J.; Wang, W.; Qin, S.; Zhang, L. Synthesis of multi-walled carbon nanotube supported nickel catalysts by hydrazine reduction and their electrocatalytic activity on ethanol electro-oxidation. *Mater. Lett.* **2011**, *65*, 3396−3398.
(27) Ren, L.; Hui, K. S.; Hui, K. N. Self-assembled free-standing three-dimensional nickel nanoparticle/graphene aerogel for direct ethanol fuel cells. *J. Mater. Chem. A* **2013**, *1*, 5689−5694.
(28) Jin, G. P.; Ding, Y. F.; Zheng, P. P. Electrodeposition of nickel nanoparticles on functional MWCNT surfaces for ethanol oxidation. *J. Power Sources* **2007**, *166*, 80−86.
(29) Yang, J.; Tan, J.; Yang, F.; Li, X.; Liu, X.; Ma, D. Electro-oxidation of methanol on mesoporous nickel phosphate modified GCE. *Electrochem. Commun.* **2012**, *23*, 13−16.
(30) Danaee, I.; Jafarian, M.; Forouzandeh, F.; Gobal, F.; Mahjani, M. G. Electrocatalytic oxidation of methanol on Ni and NiCu alloy modified glassy carbon electrode. *Int. J. Hydrogen Energy* **2008**, *33*, 4367−4376.
(31) Song, J. H.; Yu, J. Y.; Zhang, M. Z.; Liang, Y. J.; Xu, C. W. Glycerol electrooxidation on Au/Ni core/shell three-dimensional structure catalyst. *Int. J. Electrochem. Sci.* **2012**, *7*, 4362.
(32) Holade, Y.; Morais, C.; Servat, K.; Napporn, T. W.; Kokoh, K. B. Toward the electrochemical valorization of glycerol: Fourier transform infrared spectroscopic and chromatographic studies. *ACS Catal.* **2013**, 3, 2403−2411.
(33) Climent, V.; García-Aríá, N.; Feliu, J.-M. In *Fuel Cell Catalyst, A Surface Science Approach*; Koper, M. T. M., Ed.; Wiley: Hoboken, NJ, 2009; pp 209−244.
(34) Bhattacharjee, D.; Chowdhury, S. R.; Bhattacharya, S. K.; Dasgupta, S. Room temperature synthesis of $Pd_x Ni_{100-x}$ nanoalloy: superior catalyst for electro-oxidation of methanol and ethanol. *J. Appl. Electrochem.* **2019**, *49*, 681−691.
(35) Watanabe, M. A.; Motoo, S. Electrocatalysis by ad-atoms: Part II. Enhancement of the oxidation of methanol on platinum by ruthenium ad-atoms. *J. Electroanal. Chem. Interfacial Electrochem.* **1975**, *60*, 267−273.
(36) Houache, M. S. E.; Hughes, K.; Safari, R.; Botton, G. A.; Baranova, E. A. Modification of Nickel Surfaces by Bismuth: Effect on Electrochemical Activity and Selectivity toward Glycerol. *ACS Appl. Mater. Interfaces* **2020**, *12*, 15095−15107.
(37) Houache, M. S. E.; Hughes, K.; Ahmed, A.; Safari, R.; Liu, H.; Botton, G. A.; Baranova, E. A. Electrochemical valorization of glycerol on Ni-rich bimetallic NiPd nanoparticles: Insight into product selectivity using in situ polarization modulation infrared-reflection absorption spectroscopy. *ACS Sustainable Chem. Eng.* **2019**, *7*, 14425−14434.
(38) Jhong, H. R. M.; Brushett, F. R.; Kenis, P. J. The effects of catalyst layer deposition methodology on electrode performance. *Adv. Energy Mater.* **2013**, *3*, 589−599.
(39) Hori, Y.; Wakebe, H.; Tsukamoto, T.; Koga, O. Electrocatalytic process of CO selectivity in electrochemical reduction of CO_2 at metal electrodes in aqueous media. *Electrochim. Acta* **1994**, *39*, 1833−1839.
(40) Baranova, E. A.; Le Page, Y.; Ilin, D.; Bock, C.; MacDougall, B.; Mercier, P. H. Size and composition for 1−5 nm Ø PtRu alloy nanoparticles from Cu Kα X-ray patterns. *J. Alloys Compd.* **2009**, *471* (1−2), 387−394.
(41) Tahmasebi, S.; Jahangiri, S.; Mosey, N. J.; Jerkiewicz, G.; Mark, A. F.; Cheng, S.; Botton, G. A.; Baranton, S.; Coutanceau, C. Remarkably Stable Nickel Hydroxide Nanoparticles for Miniaturized Electrochemical Energy Storage. *ACS Applied Energy Materials* **2020**, DOI: 10.1021/acsaem.0c00483.
(42) Ahila, M.; Malligavathy, M.; Subramanian, E.; Pathinettam Padiyan, D. Effect of anodization time on the growth of twinned pyramid crystals of bismite from polyhedral bismuth particle by facile electrolysis-based oxidation. *Part. Sci. Technol.* **2018**, *36*, 655−659.
(43) Ding, W.; Li, L.; Xiong, K.; Wang, Y.; Li, W.; Nie, Y.; Chen, S.; Qi, X.; Wei, Z. Shape fixing via salt recrystallization: a morphology-controlled approach to convert nanostructured polymer to carbon nanomaterial as a highly active catalyst for oxygen reduction reaction. *J. Am. Chem. Soc.* **2015**, *137*, 5414−5420.
(44) Biesinger, M. C.; Lau, L. W.; Gerson, A. R.; Smart, R. S. C. The role of the Auger parameter in XPS studies of nickel metal, halides and oxides. *Phys. Chem. Chem. Phys.* **2012**, *14* (7), 2434−2442.
(45) Biesinger, M. C.; Payne, B. P.; Lau, L. W.; Gerson, A.; Smart, R. S. C. X-ray photoelectron spectroscopic chemical state quantification of mixed nickel metal, oxide and hydroxide systems. *Surf. Interface Anal.* **2009**, *41* (4), 324−332.
(46) Shin, H. U.; Lolla, D.; Nikolov, Z.; Chase, G. G. Pd−Au nanoparticles supported by TiO_2 fibers for catalytic NO decomposition by CO. *J. Ind. Eng. Chem.* **2016**, *33*, 91−98.
(47) Yang, S.; Dong, J.; Yao, Z.; Shen, C.; Shi, X.; Tian, Y.; Lin, S.; Zhang, X. One-pot synthesis of graphene-supported monodisperse Pd nanoparticles as catalyst for formic acid electro-oxidation. *Sci. Rep.* **2015**, *4*, 4501.
(48) Ebrahimpour, Z.; Mansour, N. Annealing effects on electrical behavior of gold nanoparticle film: Conversion of ohmic to non-ohmic conductivity. *Appl. Surf. Sci.* **2017**, *394*, 240−247.
(49) Chu, L.; Zhang, J.; Wu, Z.; Wang, C.; Sun, Y.; Dong, S.; Sun, J. Solar-driven photocatalytic removal of organic pollutants over direct Z-scheme coral-branch shape Bi_2O_3/SnO_2. *Mater. Charact.* **2020**, *159*, 110036.
(50) Oprea, B.; Radu, T.; Simon, S. XPS investigation of atomic environment changes on surface of B2O3−Bi2O3 glasses. *J. Non-Cryst. Solids* **2013**, *379*, 35−39.
(51) Cossar, E.; Oyarce Barnett, A.; Seland, F.; Baranova, E. A. The performance of nickel and nickel-iron catalysts evaluated as anodes in anion exchange membrane water electrolysis. *Catalysts* **2019**, *9*, 814.
(52) Yang, R.; An, L.; Zhang, Y.; Zhang, N.; Dai, T.; Xi, P. Atomic Insights of Iron Doping in Nickel Hydroxide Nanosheets for Enhanced Oxygen Catalysis to Boost Broad Temperature Workable Zinc− Air Batteries. *ChemCatChem* **2019**, *11*, 6002−6007.
(53) Trasatti, S.; Petrii, O. A. Real surface area measurements in electrochemistry. *Pure Appl. Chem.* **1991**, *63*, 711−734.
(54) Pittayaporn, N.; Therdthianwong, A.; Therdthianwong, S. Au/C catalysts promoted with Ni for glycerol electrooxidation in alkaline media. *J. Appl. Electrochem.* **2018**, *48*, 251−262.
(55) Luo, M.; Guo, S. Strain-controlled electrocatalysis on multimetallic nanomaterials. *Nat. Publ. Rev.* **2017**, *2*, 17059.
(56) Inoue, H.; Kimura, S.; Teraoka, Y.; Chiku, M.; Higuchi, E.; Lam, B. T. X. Mechanism of glycerol oxidation reaction on silver-modified palladium electrode in alkaline medium. *Int. J. Hydrogen Energy* **2018**, *43*, 18664−18671.
(57) Simões, M.; Baranton, S.; Coutanceau, C. Electro-oxidation of glycerol at Pd based nano-catalysts for an application in alkaline fuel

cells for chemicals and energy cogeneration. *Appl. Catal., B* **2010**, *93*, 354−362.
(58) Dai, C.; Sun, L.; Liao, H.; Khezri, B.; Webster, R. D.; Fisher, A. C.; Xu, Z. J. Electrochemical production of lactic acid from glycerol oxidation catalyzed by AuPt nanoparticles. *J. Catal.* **2017**, *356*, 14−21.
(59) González-Cobos, J.; Baranton, S.; Coutanceau, C. Development of bismuth-modified PtPd nanocatalysts for the electrochemical reforming of polyols into hydrogen and value-added chemicals. *ChemElectroChem.* **2016**, *3*, 1694−1704.
(60) Kenis, P.; Nwabara, U. O.; Cofell, E. R.; Verma, S.; Negro, E. Durable Cathodes and Electrolyzers for the Efficient Aqueous Electrochemical Reduction of CO_2. *ChemSusChem* **2020**, *13*, 855.
(61) Verma, S.; Kim, B.; Jhong, H. R. M.; Ma, S.; Kenis, P. J. A gross-margin model for defining technoeconomic benchmarks in the electroreduction of CO_2. *ChemSusChem* **2016**, *9*, 1972−1979.
(62) Jouny, M.; Luc, W.; Jiao, F. General techno-economic analysis of CO_2 electrolysis systems. *Ind. Eng. Chem. Res.* **2018**, *57*, 2165−2177.
(63) Market Data of Gold; https://www.nasdaq.com/market-activity/commodities/gc%3Acmx (accessed on January 2020).
(64) Market Data of Platinum; https://www.nasdaq.com/market-activity/commodities/pl%3Anmx (accessed on January 2020).
(65) London Metal Exchange Nickel Official Prices; https://www.lme.com/enGB/Metals/Non-ferrous/Nickel#tabIndex=0 (accessed on January 2020).

https://dx.doi.org/10.1021/acsaem.0c01282
ACS Appl. Energy Mater. 2020, 3, 8725−8738